

Hypermultiplexed Integrated Tensor Optical Processor

Shaoyuan Ou¹, Alexander Sludds², Ryan Hamerly^{2,4}, Ke Zhang³, Hanke Feng³, Eric Zhong¹, Cheng Wang³, Dirk Englund², Mengjie Yu¹, Zaijun Chen^{1*}

¹*Ming Hsieh Department of Electrical and Computer Engineering, University of Southern California, Los Angeles, CA 90089, USA*

²*Research Laboratory of Electronics, MIT, Cambridge, MA 02139, USA*

³*Department of Electrical Engineering & State Key Laboratory of Terahertz and Millimeter Waves, City University of Hong Kong, Kowloon, Hong Kong, China*

⁴*PHI Laboratories, NTT Research Inc., 940 Stewart Drive, Sunnyvale, CA 94085, USA*

*Email: zaijunch@usc.edu

Optical processors hold great potential to accelerate deep learning tasks with their high clock-rates and low-loss data transmission. However, existing integrated systems are hindered by low scalability due to the quadratic scaling of device counts, energy costs with high-speed analog-to-digital converters, and lack of inline nonlinearity. Here, we overcome these challenges with a wavelength-space-time multiplexed optical tensor processor. Hyperdimensional parallelism allows matrix-matrix multiplications (N^3 operations) using $O(N)$ devices. We incorporated wavelength-multiplexed III/V-based micron-scale lasers (spanning ~ 1 THz) for input activation with inline rectifier (ReLU) nonlinearities and thin-film Lithium-Niobate electro-optic modulators ($V_{\pi} \approx 1.3$ V) for dynamic weighting. With each device encoding 10-billion activations per second, we demonstrated a machine-learning model with 405,000 parameters. High-clock-rate (10 GS/s), low-energy (500 fJ/OP) parallel computing with real-time programmability unlocks the full potential of light for next-generation scalable AI accelerators.

Preprint at arXiv. January 31, 2024

Introduction

Tensor processors, with their unique prowess in data-intensive algorithms, have become a major computing building block in modern high-performance computing (HPC) and artificial intelligence (AI), leading science and technology innovations in deep learning (1) for language processing (2), image analysis (3) and automation (4), NP-hard optimization (5) for scheduling, route planning, and resource allocation, and iterative solvers (6) for multiphysics simulation (7) and cryptocurrency (8) (Fig. 1a). In particular, recent success in large language models (LLMs) (9) has made AI available in our daily lives, improving our work efficiency and convenience (10). Typically, LLMs with up to a trillion parameters (GPT-4, as of 2023 (11)) are trained with trillions of input tokens (texts or codes), each computes with the model parameters leading to demanding requirements in computing hardware, energy cost, and training times (up to several months (11)). The computing power requirement has become the fundamental bottleneck in the further development and deployment of AI models.

Due to the massive memory interface requirements in tensor processing (12), traditional Von-Neumann architectures are inefficient in performing these tasks. New computing paradigms (Fig. 1b), harnessing various types of intrinsic parallelism, are in active development. The main figures of merit to optimize are (F1) the computing power—the number of operations per second, (F2) energy efficiency—the energy consumption per

operation, (F3) computing density—the number of operations per chip area per second, and (F4) model scalability – number of parameters supported by the optical system.

Complementary-metal-oxide-semiconductor (CMOS) circuits, such as graphic processing units (GPUs) (13), tensor processing units (TPUs) (14), and application-specific integrated circuits (ASICs) (15), are the current workhorse in HPC. The high performance of CMOS processors derives from small feature sizes and a tailored system for memory communication, for instance, each input data is fed to N processing elements (PEs) via electronic wires to improve the data bandwidth with parallel processing (Fig. 1b); however, the energy efficiency and clock rate scale inversely with the number of PEs due to wire capacitance ($E_w \propto CV^2$), which has become the fundamental bottleneck of CMOS electronics (16). Quantum parallelism (17) is another attractive platform with exponential speedups in computation speed, but these systems are very tied to certain problems and their realization and scalability have been a long-term obstacle.

Optics is emerging with the promise to improve the computing figures of merit by many orders of magnitude, owing to nearly loss-less propagation, large optical bandwidth, and a unique combination of optical degrees of freedom (space, wavelength, polarization, etc) for parallel processing (Fig. 1b). Recent progress has shown matrix-vector multiplications (MVMs) with the potential of speed-of-light computation (18–20), free-space data parallel processing (21–24) and on-chip integration (25–30). However, existing techniques based on Mach-Zehnder-Interferometer meshes (25–27), phase change material (PCM) crossbars (30, 31), or spatial light modulators (19, 21, 22, 29) require $O(N^2)$ photonic devices to map a matrix in space and high-speed readout electronics to improve the throughput, leading to chip area and energy costs hindering their scalability for on-chip integration. Moreover, to fully unlock the potential of optical processing, matrix-matrix multiplication (MMM) with cubic operations enables better throughput and efficiency scaling than MVMs, but its realization is challenging due to the three-dimensional (3D) data structure. The potential of MMMs has recently been explored with a PCM crossbar (with 4×4 model parameters) (30, 31), though at the cost of using $O(N^2)$ optical wavelengths (30) or radio-frequency multiplexing (31) with energy-consuming high-speed electronics. A compact, low energy integrated optical system with high model scalability is yet to be developed.

Here we propose and demonstrate a hypermultiplexed integrated tensor optical processor (HITOP), based on space-, time-, and wavelength-domain 3D data encoding (Fig. 1c). The system is built on the thin-film lithium niobate (TFLN) platform with ultralow-energy electro-optic modulators for weight streaming. The input data are injected to HITOP with arrays of wavelength-multiplexed vertical-cavity surface-emitting lasers (VCSELs) based on Indium Phosphide (InP) as the gain medium. Spatial fanout with on-chip beam routing and spectral fanout with wavelength-division multiplexing (WDM) enable in-plane neural connectivity for compact system integration. A rectified linear unit (ReLU) nonlinearity, based on the VCSEL lasing threshold effect, is incorporated without additional energy cost. Leveraging time-domain data activation, HITOP operates at the clock rate of 10 GS/s encoding 10 billion parameters per second (each device), thus allowing it to operate large network models at low device counts. The energy efficiency is improved with high parallelism using fanout and fan-in amortization.

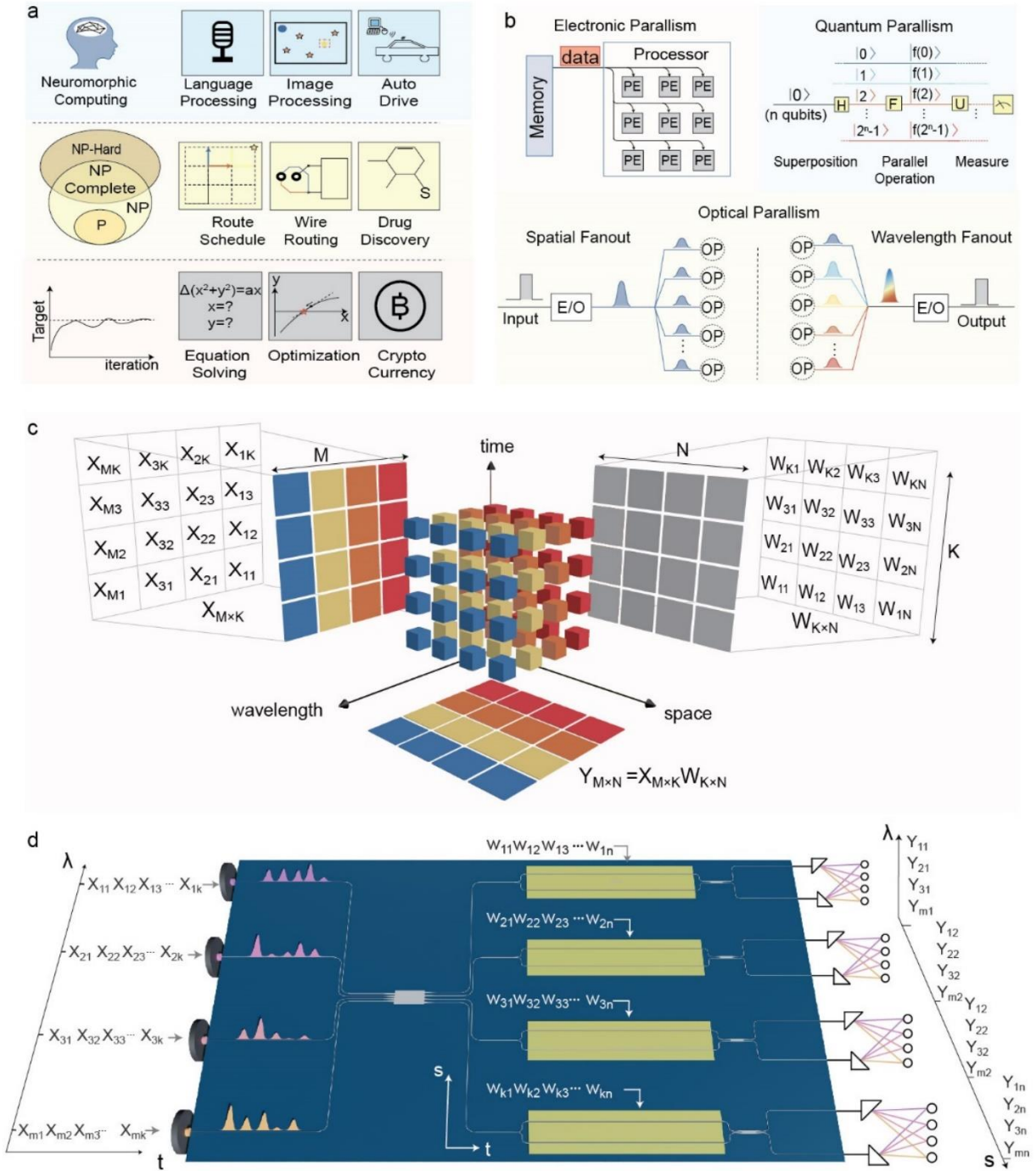


Fig 1. HITOP concept. (a) Tensor processing in HPC for neuromorphic computing, NP-hard solvers, and iterative solvers. (b) Comparison of various emerging computing platforms, utilizing data parallelism, quantum parallelism, and optical parallelism. PE: processing unit. H: Hadamard gate. F: operating function. U: unitary operator. OP: operation. (c) HITOP data format based on space-, time- and wavelength three-dimensional data encoding. The input matrix $X_{M \times K}$ is encoded in time-wavelength dimensions with data fanout in space; the weight matrix is time-space encoded with fanout in wavelength. Dot products of overlapping elements are integrated over the time axis to lay out the MMM results in wavelength-space dimensions. (d). Chip-based architecture of HITOP showing 4 micron-scale laser wavelength channels for input matrix $X_{M \times K}$ encoding and 4 spatial TFLN modulators for weighting.

Table 1 State-of-the-art Photonic-chip-based computing systems

Reference	Technology	Operation	Hardware	Parallelism	Model scalability
Shen 2017 (26)	MZI mesh	MVM	N^2 MZIs	1/MZI	# of MZIs
Tait 2017(28)	WDM microring weight bank	MVM	N^2 microrings + 1 modulator	1/microring N/MZM	# of microrings
Ashtiani 2022(32)	Silicon attenuators	VVM	N attenuators	1/attenuator	# of attenuators
Xu 2021(29)	Comb+ Chromatic dispersion	MVM	N^2 SLM pixels + 1 modulator	N/modulator 1/SLM pixel	# of SLM pixels
Feldmenn 2021 (30)	WDM+PCM crossbar	MMM	N^2 Comb lines + N^2 modulators + N^2 PCMs + 2^N power loss	N/PCM, N/modulator	# of PCMs
Dong 2023(31)	RFM+WDM+PCM crossbar	MMM	N RF tones + N modulators + N^2 PCMs + 2^N power loss	N/PCM N/modulator	# of PCMs
Chen 2023(23, 33)	Homodyne VCSEL arrays	MVM	N VCSELS + injection locking	N/input VCSEL 1/ weight VCSEL	# of VCSELS x clock rate
HITOP (this work)	WDM VCSELS + TFLN MZMs	MMM	N VCSELS + N modulators	N/VCSEL N/modulator	# of LN modulators x clock rate

HITOP architecture

HITOP is a hybrid optoelectronic system that performs general-purpose tensor processing $Y_{(M \times N)} = X_{(M \times K)} W_{(K \times N)}$ (Fig. 1c and d), where M, K, N denote the matrix sizes (with m, k, n being the matrix indices). Here the input matrix $X_{(M \times K)}$ is mapped to the wavelength-time bases, where the m -th vector (size $1 \times K$) is amplitude encoded at the m -th laser wavelength with K time steps, $E(\lambda_m, t_k) = X_{m,k}$. This wavelength-time encoding format has been exploited in our previous work in edge computing (34) for network model transmission. Here for on-chip tensor processing, we combine a total of M wavelength channels via broadband multimode interferometers (MMIs) or wavelength division multiplexers. The combined beam is spatially fanout with on-chip beam routing to N spatial copies. At the S_n -th channel, the beam passes through a broadband optical modulator encoding a weight vector W_n in K time steps $E(t_k, S_n) = W_{k,n}$ to all the M wavelengths. The cascaded modulation leads to multiplication on laser intensity $E(\lambda_m, t_k, S_n) = X_{m,k} W_{k,n}$. At the receiver side, each S_n -th beam is wavelength demultiplexed on M photodetectors. The resulting photocurrents are accumulated over K time steps using a charge integrating amplifier, yielding

$$Y_{m,n} = \sum_{k=1}^K E(\lambda_m, t_k, S_n) = \sum_{k=1}^K X_{m,k} W_{k,n} \quad (1)$$

at the m -th wavelength of the n -th spatial output.

The key advantages of our architecture are the system simplicity, scalability, and energy efficiency enabled by parallel processing with hyperdimensional multiplexing. Utilizing the time axis as the common dimension for matrix encoding (Fig. 1c), HITOP allows MMM

operations with M wavelengths and N spatial modes. The number of encoding devices is linear with $O(M+N)$, which is in contrast to the $O(N^2)$ requirement in other photonic (25–30) and electronic systems (16). Therefore, this architecture is simplified and scales much better. Similar to other techniques of MMM (30, 31), an $O(N^2)$ scaling of readout components is required to scale up the system throughput. Unlike these systems where high-speed electronics (e.g., transimpedance amplifiers (TIAs), analog-to-digital converters (ADCs)) are required and have become the bottleneck in energy efficiency, HITOP only reads out after integrating over K clock cycles, thus significantly reducing the requirements for high-speed readout electronics.

Results

HITOP device platform

A key requirement of HITOP is high-speed input encoding using a compact, scalable multi-wavelength laser source. We explore wafer-fabricated III/V-semiconductor VCSEL transmitters (Fig. 2b), due to their state-of-the-art performance in data transmission speeds (>45 GHz (36)) and power efficiency (wall-plug efficiency (WPE) $>57\%$ (37)). Our VCSELs are fabricated at VI Systems GmbH (Berlin, Germany) with InAlGaAs/InP multilayer quantum wells as the active gain medium with emission wavelengths around 1550 nm (38, 39). A 300-mm wafer consisting of 100,000 VCSELs with a pitch of 250 μm is shown in Fig. 2a. Each VCSEL is packaged with an electronic wire bond to an external driver for data modulation, and the output is coupled to a single mode fiber for WDM and edge coupling to the TFLN chips. The VCSELs are designed to emit at distinct center wavelengths around 1545 nm, 1550 nm and 1555 nm at room temperature, with a thermal tuning range of ± 2 nm to cover the whole spectrum of >10 nm. Seven VCSELs are tuned to match a standard telecommunication WDM grid (Fig. 2d), with a total optical bandwidth of 6 nm (0.7 THz) from (1547 nm to 1553 nm). The lasing threshold voltage is 1.2 V and each VCSEL emits >1 mW of optical power with a WPE of 20%. The 3 dB signal modulation bandwidth of each VCSEL exceeds 10 GHz (Fig. 2k). Random data modulation with VCSELs achieved an encoding error of $<0.3\%$, corresponding to >8 bits precision (Supplementary).

Another challenge to HITOP is to develop a broadband, low-loss and scalable photonic platform for high-speed weight matrix encoding at CMOS-compatible driven voltages. The TFLN platform has emerged as a practical solution to overcome the current trade-off limitations (in bandwidth, loss, and V_π) of silicon photonics and combines the superior Pockels properties and scalable fabrication capabilities for the next generation of integrated optoelectronic circuits (40). A similar footprint, the performance of an EO-based Pockels modulator has overperformed the silicon or InP modulator in terms of lower switching voltage and optical loss, higher extinction ratio and EO bandwidth as well as better linearity, all of which are essential to HITOP devices with lower energy consumption, higher throughput and precision (41). In addition, the thin film platform could be engineered to support ultrawide optical bandwidth thanks to the dispersion engineering of tightly confined waveguides, precision nanolithography and compact device sizes as compared to bulk EO modulators. The TFLN Mach Zehnder modulator (MZM) in our HITOP device performs weight streaming and time-wise dot products simultaneously with a broad range of wavelengths using a traveling waveguide design, providing a >40 GHz electro-optical bandwidth with a $V_\pi=1.3$ V (2-cm length). The modulators are slightly unbalanced with a free spectral range >150 nm (Supplementary). To keep the modulator in a quasi-linear region,

we send input data with a peak-to-peak voltage of 0.6 V, corresponding to ~ 88 fJ/Symbol (Methods). TFLN modulators have $<0.4\%$ data encoding error, corresponding to 8 bits of precision (Supplementary Fig. S4). As amplitude modulation with optical power is positive but both positive and negative values are necessary in neural networks, we developed a modulation format in HITOP with dual-port TFLN MZMs with differential detection (Methods).

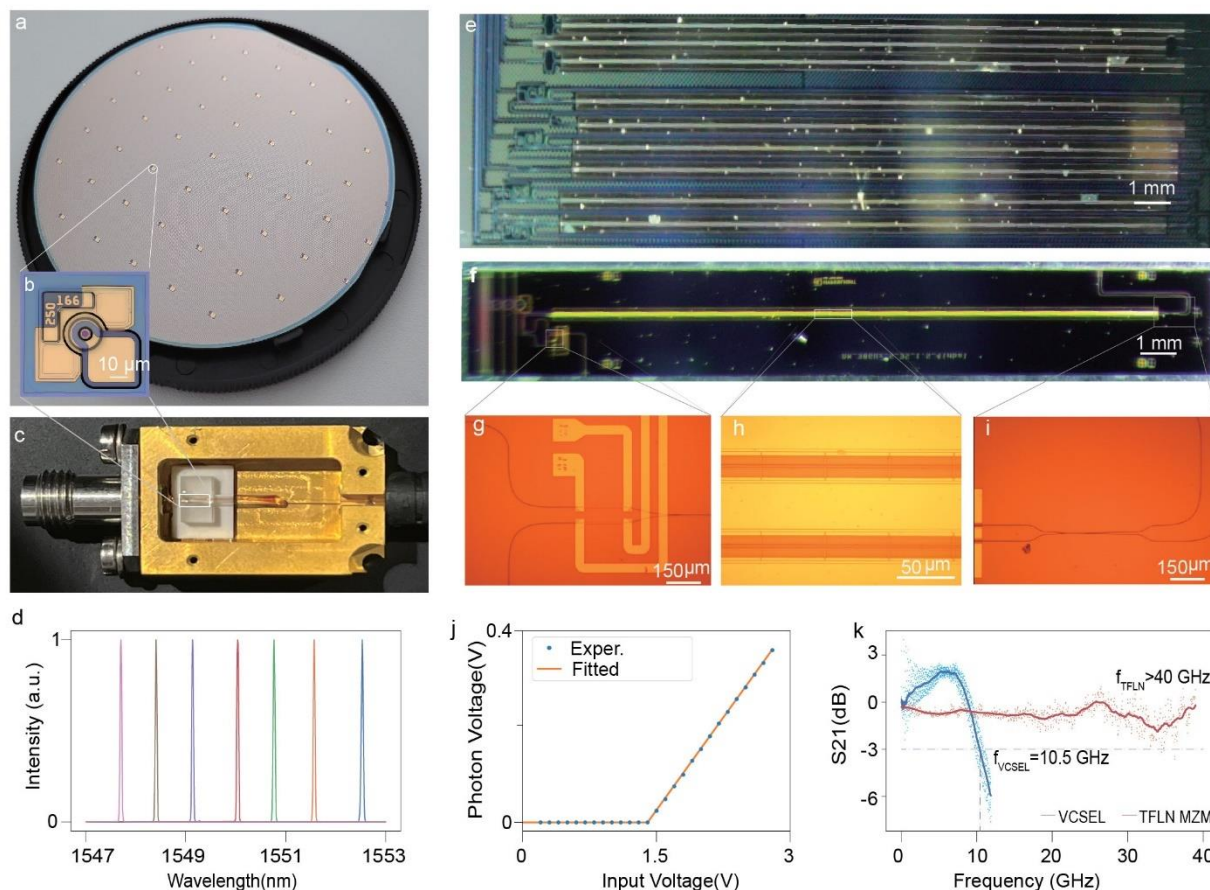


Fig 2. HITOP device platform. a. Wafer-scale fabricated VCSELs. A 3-inch wafer (VI system, Germany) with $>100,000$ single-mode VCSEL emitters, each with a 3 dB bandwidth >10.5 GHz. b: a single VCSEL laser with a footprint of $250 \times 250 \mu\text{m}$. c. A packaged VCSEL with electric wire bonds and fiber coupling. d. a spectrum with 7 VCSEL wavelengths used in HITOP, spanning 5 nm (0.7 THz). e. A fabricated TFLN chip with 9 electro-optic intensity modulators. f. An example of a 2-cm TFLN dual-output electro-optic intensity modulator. g. magnification view of heaters for setting operation bias. h. segmented electrodes for matching the microwave index and optical index (35). i. dual-port outputs. j. VCSEL threshold effect for ReLU nonlinear activation between neural network layers. Data is measured with a photodetector with a TIA. A linear fit to the experimental data results in a statistical error of 0.26%. k. radio-frequency response of TFLN modulators with 3-dB bandwidth >40 GHz and VCSELs with a bandwidth of 10.5 GHz.

HITOP benchmarking

We constructed a computing system (Methods) with 7 VCSELs and 7 broadband amplitude modulators on the fabricated TFLN chip (Fig. 4a). The VCSELs can be either biased at the lasing threshold voltage to encode positive values (input layer), or below the threshold to activate the ReLU nonlinear function (hidden layers). The inline nonlinearity would allow cascading multiple layers without converting the partial sums to digital memories. The TFLN

modulators are set at the quadrature point to encode positive and negative weight values. The HITOP computing accuracy is validated by sending two sets of 1000 normally distributed random values to the VCSELs and the TFLN modulators (Fig. 3a). Due to the high linearity of our transmitters, amplitude multiplication via cascaded modulation achieves good consistency (without any calibration required). The errors between the measurement and the ground truth exhibit a standard deviation of 1.5% at 100 MS/s, corresponding to a computing accuracy of 6 bits (Fig. 3b-d).

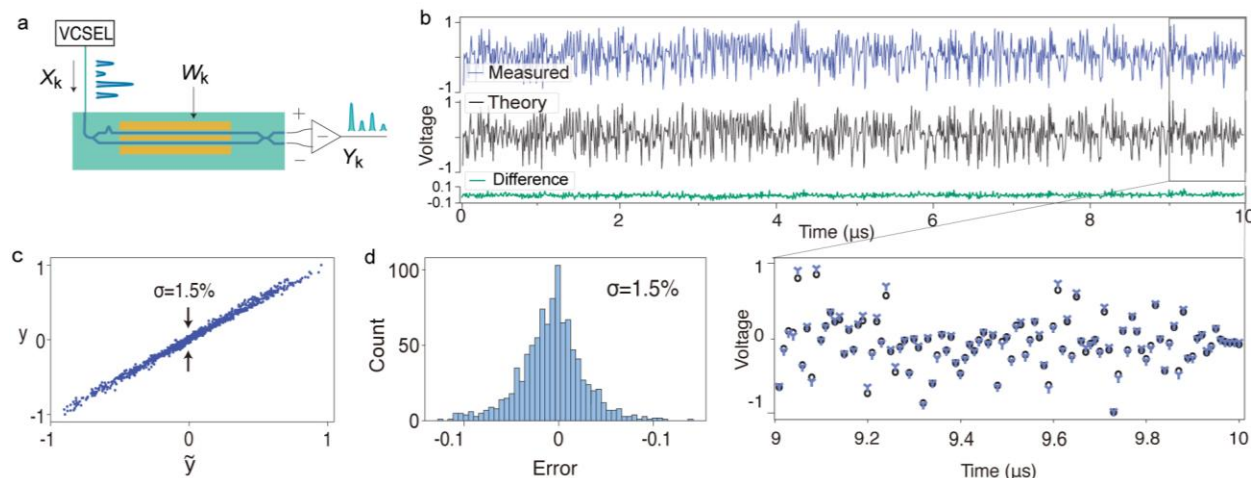


Fig 3. Experimental verification of HITOP computing accuracy. a. A vector computing unit consisting of a VCSEL and a modulator for cascaded modulation. b. Experimental results of multiplication of 2 random-distributed vectors with negative and positive weights. c. correlation of expected values and experimental multiplication results. d. histogram of the multiplication errors between ground truth and experimental results.

HITOP is scalable with high-speed time-domain data modulation. Operating at 10 GS/s, each VCSEL encodes 10 billion activations per second. The multiplication accuracy is ~ 5 bits at the clock rate of 10 GS/s (Fig. 4b). We attribute the 1-bit decrease in accuracy to the slight impedance mismatch in our driving electronics, which can be overcome with custom circuit designs. This accuracy is sufficient in our neural network inference, where each image with 28×28 pixels is flattened and encoded over times of 78.4 ns using VCSELs. The pre-trained network consists of one-layer ($28 \times 28 \rightarrow 10$) with 10 weight vectors using TFLN modulators. We implemented an integrating charge amplifier (Methods) at each photo-receiver to accumulate the currents generated from each vector multiplication. No crosstalk was observed due to high channel separation in the WDM channels (100 GHz channel width). High classification accuracy is observed at the seven wavelength channels (Methods), achieving $\sim 97\%$ of digital accuracy (Fig. 3e).

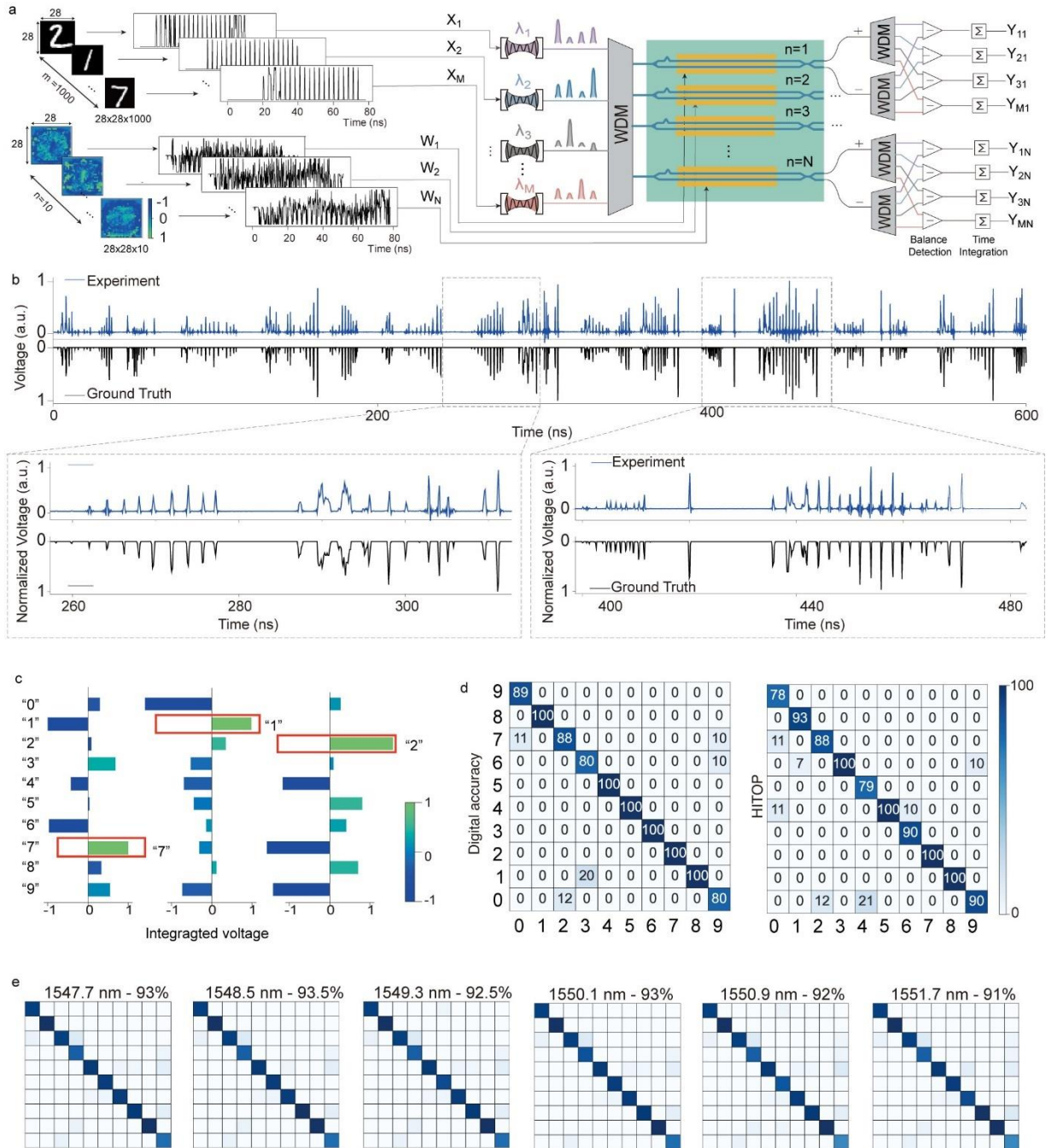


Fig 4. HITOP benchmarking with MNIST hand-written digit classification. a. Implementation of a single-layer pre-trained neural network model. The 10 weight vectors are flattened and streamed on the TFLN modulators. The images are encoded to VCSEL transmitters. b. a time trace multiplication result for digit classification with 10 GS/s data rate, the zoom-in figures show the time trace with great consistency to the digital multiplication. c. time-integrated voltages of 3 wavelength channels at the output of 10 spatial modes. d and e. Confusion matrix for MNIST digit classification at seven different wavelength channels showing good classification accuracy (with numbers in supplementary) as the digital model.

HITOP is a versatile architecture that can be reprogrammed for different tasks. We operate different MNIST data sets for digital (Methods), fashion, and letter classification. With a three-layer network model (size 28x28→100→10) and ReLU inline nonlinear activations (Supplementary), HITOP successfully classified over 91.8% among the 1000 random Fashion

images (Fig. 5). Reprogramming for the letter classification with the EMNIST letter dataset with 26 classification levels, HITOP achieved 93.1% classification accuracy over 5000 images with a total of 4,050,000,000 operations. The model size is $28 \times 28 \rightarrow 500 \rightarrow 26$, consisting of a hidden layer with 500 neurons, with a total of 405,000 parameters, which is 25,000 more than previous integrated optical systems (Table E2).

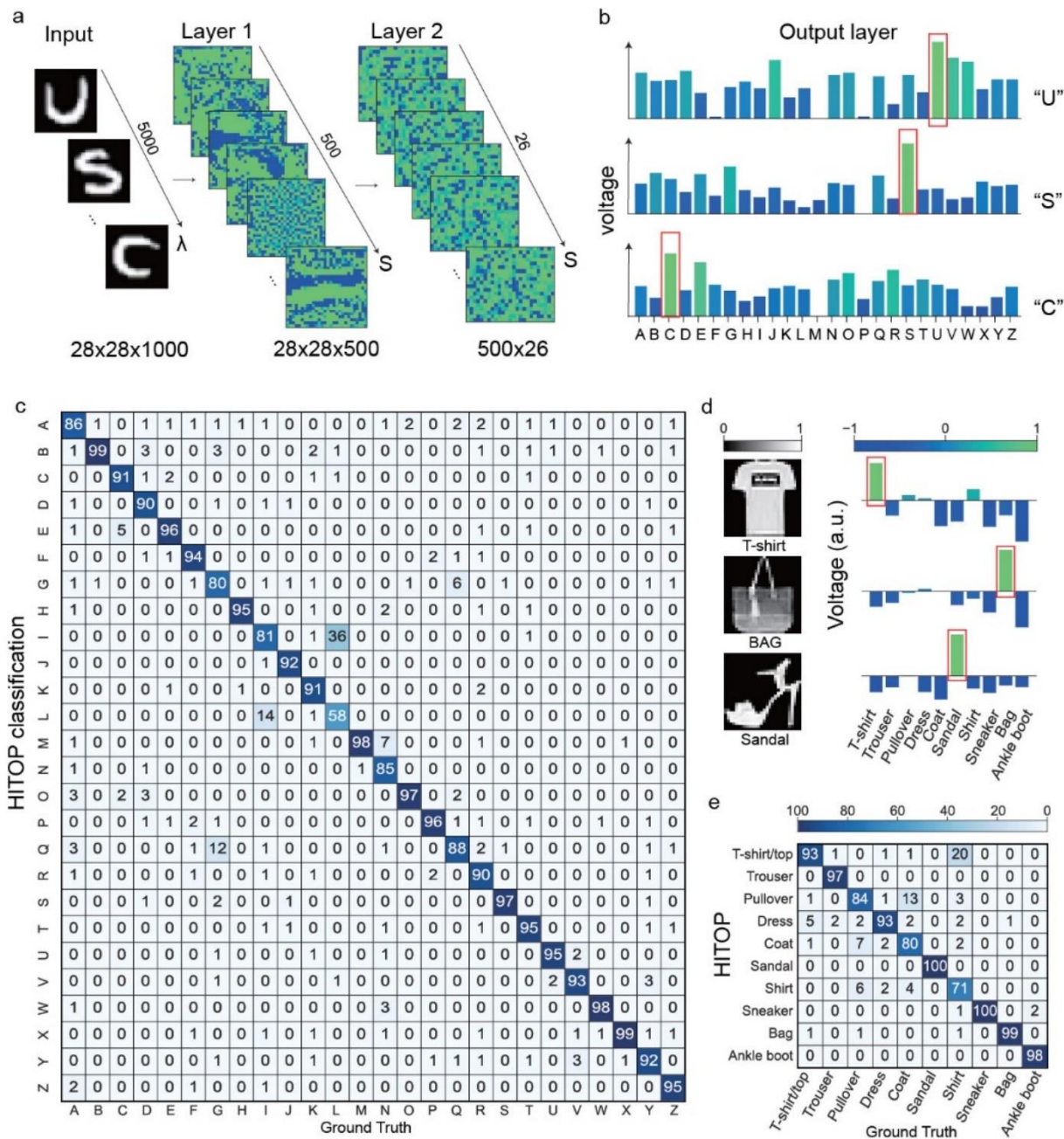


Fig 5. Experimental benchmarking of HITOP for different image classification tasks. a. Two hidden layers for the EMNIST letter classification with a network size of $28 \times 28 \rightarrow 500 \rightarrow 26$. b. The read-out voltages resulting from the HITOP output layer with high voltages for the letters “U”, “S” and “C”. c. Confusion matrix for EMNIST letter classification with a test set of 5000 images showing a classification accuracy of 93.1%. d.

Fashion MNIST classification with a network size of $28 \times 28 \rightarrow 100 \rightarrow 26$. Experimental result of 3 example images. e. a confusion matrix for 1000 Fashion MNIST test images achieved an experimental accuracy of 91.8%.

System performance

We experimentally demonstrated HITOP with wavelength multiplexed VCSELs ($M=7$ wavelength channels spanning around 1 THz) incorporating onto the TFLN platform with $N=7$ modulators at the clock rate of 10 GS/s. The performance is validated with neural network benchmarking of digital, fashion, and letter classifications. Hyperdimensional parallel operations improved our system performance in computing throughput, energy efficiency, area density, and model scalability. (F1) We achieved a throughput (T) of $T=2 \cdot M \cdot N \cdot R=1.12$ TOPS, which can be scaled up quadratically with high device counts (Discussion). (F2) HITOP utilized parallel processing to amortize the energy cost. The energy consumption in data input (e.g. digital-to-analog converts) is amortized by the fanout factor of N or M , while that for readout electronics is amortized with a fan-in integration (factor of K). The full-system energy cost can reach ~ 0.5 pJ/OP with appropriate circuit design (Methods and Table E1), which is 2x better than the electronic barrier of 1 pJ/OP. (F3) The chip area density (σ) is dominated by the size of the TFLN broadband modulators (20×0.4 mm²) (Methods). Each modulator simultaneously encodes data to M wavelength channels, with a density of $\sigma=2 \times M \times R/A_2=17.5$ GOPS/mm². This can be improved by two orders of magnitude in future scaling with $M=1000$ wavelengths and a slightly more compact TFLN design (see discussion). (F4) With time-multiplexed data encoding, the network model scales with the number of devices and the system clock rates. As demonstrated, each TFLN modulator inputs 10 billion weight parameters per second, which is a promising approach to scale up optical systems in the near term to operate large network models (e.g., GPT 3 with 175 billion parameters (42)). Our demonstrated model has 405,000 parameters which is 25,000x larger than those implemented in other fully integrated optical systems (30), as listed in Supplementary.

Discussion

Our proof-of-concept explores the scalability, reprogrammability, and versatility of HITOP with chip-based in-plane multidimensional multiplexing with reduced device counts while addressing the energy cost in data conversion with state-of-the-art photonic platforms. With near-term technology, the fanout factor may be scaled to $M=N=1000$, where InP-based VCSEL technology can support 1000 parallel wavelength channels (spacing of 50 GHz), as wide frequency coverage over $1.3 \mu\text{m}-2 \mu\text{m}$ has been reported (43). TFLN devices (with transparency window 350 nm-5200 nm(41, 44-46)) can support a wide spectral span and dispersion engineering (47), and TFLN modulators are currently volume manufactured on the wafer scale with high yield(48). With the improved device counts, the HITOP throughput could reach $T=20$ TOPS at the demonstrated clock rate of 10 GS/s, which is about 100x better than the best-in-class electronic systems (i.e., NVIDIA A100 or Google TPU v4 (14)). A computing density of $\sigma=10$ TOPS/mm² might be within reach when using a compact TFLN modulator layout (10×0.2 mm² per modulator). HITOP shows a clear path to reach an energy cost towards few fJ/OP (Table E1), which would overcome the electronic bottleneck by 1000 folds. Low energy cost at sub-fJ/OP might be possible when the current energy bound on electronic DACs is improved with co-packaging optical DACs (49).

HITOP with high computing power at low energy cost will usher in a new era of possibilities and transformative applications across various domains. Based on three-dimensional data streaming with dynamic reprogrammability, HITOP is suited for scalable AI computing to train models with trillions of parameters with speedup in iterations, opening up new

possibilities for larger AI models in language processing and machine vision. This also provides an eco-friendly solution to improve the processing power of smart, light-weight edge tensor processors for real-time decision making in autonomous vehicles and robots, and smart sensors in the internet of things. Beyond AI applications, the computing power will speed up simulation and modeling of complex physical and biological systems (e.g., climate changes and molecular dynamics) for accurate prediction of environmental challenges or drug discovery and healthcare.

Methods

TFLN Fabrication

The TFLN MZMs are fabricated at Hyperlight Corp and the City University of Hong Kong. The electrode is designed as a traveling waveguide for RF signals with segmented fins for optics and microwave index matching (35). Each MZM has a length of 2 cm and width of ~400 μm with dual-port output. The MZM and MMI structure is patterned through electron beam lithography. Deep reactive ion etch (DRIE) is applied to shape the TFLN waveguide with an etch depth of 350 nm. A silicon dioxide is grown as the cladding layer. Annealing reduces the TFLN waveguide loss. A laser direct write lithography is applied to define the electrode pattern. Gold electrodes are deposited using electron beam deposition.

Positive and negative weight value encoding

The MZMs are designed to have one input and two output ports with differential detection. Each MZM is biased at the quadrature point such that the input power is equally split to the 2 ports. Electro-optic data modulation draws optical power from one port to the other, creating a power difference that is proportional to the modulation voltages. The power difference (positive and negative) is converted to photo-voltages using balanced detection.

System performance.

Throughput. The HITOP throughput (T) scales with $T=2 \cdot M \cdot N \cdot R$, where M is the number of wavelengths and N is the number of spatial modes (TFLN modulators), R is the clock rate and a factor of 2 accounts for both multiplication and accumulate operations. With $M=7$ VCSEL wavelengths, $R=10$ GS/s, and a total of $N=7$ TFLN modulators, our computing throughput is $T=1.12$ TOPS. This number can be scaled up to $T=20$ POPS with $N=M=1000$ in future development.

Energy efficiency. The energy cost of each input encoding with VCSELs (or TFLN modulators) is fanned out to N spatial modes (or M wavelengths) for parallel processing (Table E1). The energy consumption of readout electronics, including analog-to-digital converters (ADCs), trans-impedance amplifiers (TIAs), and time integrators that only apply once after integrating over K time steps, is amortized by a factor of $K=28 \times 28$. Our VCSELs are biased with a DC voltage $V_{\text{VCSEL-DC}}=1.3$ V with a current $i_{th} \approx 2$ mA, which is at a near-threshold current region with 2.6 mW DC output optical power. A positive RF signal with peak-to-peak voltage of 0.6 V is sent to VCSEL with a resistance $R=650 \Omega$ consuming 70 μW for data encoding, which is equal to 7 fJ/Symbol at 10GS/s. The TFLN MZMs are biased at the quadrature point and driven within the quasi-linear region with peak-to-peak voltage $V_{pp}=0.6$ V ($V_{\pi}=1.3$ V), which yields a root-mean-square drive voltage $V_{\text{rms}}=0.2$ V. The AC signal is encoded with 50 Ω termination. Its energy per symbol is estimated as $P_{\text{MZM}}=V_{\text{rms}}^2 / (R \cdot 50$

Ω) =88 fJ/Symbol. The energy consumption for VCSEL and TFLN encoding is within the power budget for the DACs in Table E1.

Compute Density. Compared to the compact VCSEL devices ($A_1=0.06 \text{ mm}^2$ per device), the broadband TFLN modulators ($A_2=8 \text{ mm}^2$ per device) dominate the chip area, with a computing density of $\sigma_0=2 \times M \times R/A_2=17.5 \text{ GOPS/mm}^2$ with $M=7$. In future development, with $M=1000$ and $A_2=2 \text{ mm}^2$ per device, $\sigma_1=2 \times M \times R/A_2=10 \text{ TOPS/mm}^2$

Experimental setup.

The VCSELs are packaged with both electronics wire bonding and each beam is coupled to telecommunication fibers (Fig. 2c). The emission wavelengths of 7 VCSELs are tuned to match a standard telecommunication WDM grid with a channel width of 100 GHz (OPTICO 100G DWDM 8CH MUX). The combined beams are split with fiber splitters and coupled to the TFLN chip with 7 modulators via edge coupling using standard C-band single mode fibers. Due to the limited number of arbitrary waveform generators equipped (two channels of 10 GS/s (Tektronix AWG70002B), four channels of 100 MS/s (Tektronix AWG5014C) available), the data in Fig. 2d were taken at 10 GS/s. For multi-channel operation (Fig. 2e), we ran two wavelengths and two TFLN modulators simultaneously at 100 MS/s, moving the electronic probes and drivers to different channels allows us to incorporate more devices. At the output of each modulator, the wavelengths are demultiplexed and detected with differential detection (Thorlabs PDB450C). The generated photon voltage is sampled by a high-speed oscilloscope (Rohde & Schwarz RTO6 for 100MS/s and RTP134B for 10GS/s). In terms of the model benchmarking, the photon voltage is integrated using time integrating receivers and digitized with an FPGA-based data acquisition board (Alazar Tech 9416).

Time integrating receiver. The time-integrating receivers are homemade with a charge-integrating amplifier (Texas Instruments IVC102) soldered at the backend of the photodetectors. The integration is triggered on for a target integrating time steps and switched off when the trigger voltage is set to zero. When time integration is on, the capacitor accumulates photocurrents over time and converts the integrated charges to photo-voltage that can be digitized. More details are discussed in ref(34).

Neural network training

We trained our neural network models with the standard PyTorch package. The model consists of one input layer, two fully connected hidden layers, and an output layer (Fig. 4). The input layer consists of 784 neurons, corresponding to the 28×28 pixels of a full-size MNIST digit and letter fashion MNIST image. The input is passed to two fully connected hidden layers, with matrix-matrix multiplication (batch operation) to speed up the process. For digit MNIST and Fashion MNIST, the output layer consists of 10 neurons, each neuron represents a digit (from 0 to 9) or a fashion style. For the letter MNIST, the output layer consists of 26 neurons, corresponding to the 26 levels (from a to z) of classification. The prediction result of which digit is given by the number of neurons which has the largest value. We utilize the cross-entropy loss function and retrieve the gradients in each iteration in a model implemented in PyTorch. A random additional noise is introduced during the training process to enhance the robustness of the model. A large learning rate is set to start the training and is gradually reduced to optimize the accuracy. All the models are trained using Adam as the optimizer and the cross-entropy function for the loss evaluation. The model parameters are listed in Supplementary table S3.

Neural network benchmarking.

We deployed a 3-layer neural network model with a model size of $28 \times 28 \rightarrow 100 \rightarrow 10$ for MNIST digit classification and fashion classification. ReLU nonlinearity based on the lasing threshold is incorporated between two layers. Running a test set consisting of 1000 random hand-writing digit images yielded a classification accuracy of 95.5%, which is close to the model accuracy of 95.8%. For Fashion MNIST, which is a more challenging task due to the higher image complexity, the experimental accuracy of 91.8%, which is 97.3% of digital accuracy (94.3%). With a larger model size ($28 \times 28 \rightarrow 500 \rightarrow 10$) for EMNIST letter classification, an experimental accuracy of 93.1% is demonstrated compared to the digital accuracy of 93.4%.

References and Notes

Acknowledgments: This work is supported by the DARPA NaPSAC program under project No. N66001-24-2-4002. Z.C. and M.Y. acknowledge the Optica Foundation for the challenge awards. Z.C. thanks Dr. Nikolay Ledentsov Jr. from VI Systems for supporting the VCSEL samples and useful discussion. D.E. acknowledged the Army Research Office under grant number W911NF17-1-0527, and NTT research under project number 6942193 and the NTT Netcast award 6945027. C.W. acknowledge Research Grants Council, University Grants Committee under project C1002-22Y.

Author contributions: Z.C. and M.Y. conceived and supervised the project. S.O. performed the experiment and finalized the experimental results, assisted by A.S. and R.H., A.S. developed the integrating receivers. S.O. and E.Z. created the software model for neural network training. K.Z., H.F., and C.W. fabricated the TFLN MZMs. D.E. provided the experimental support and discussions. Z.C. and S.O. wrote the manuscript with contributions from all the authors.

Competing interests: Z.C, S.O. and M.Y. have filed a patent related to HITOP, bearing application 064189-0980(2023-049-01). D.E. serves as scientific advisor to and holds equity in Lightmatter Inc. A.S. is a senior photonic architect at Lightmatter Inc. and holds equity. Other authors declare no competing interests.

Data and materials availability: Data and materials are available from the corresponding author upon reasonable request.

Extended tables:

Table E1 Energy consumption of electronic driving circuits of HITOP

Components	Energy budget	Parallelism† (Now)	Energy/OP	Parallelism (Future development)	Energy/OP
VCSEL DC driving	2.6 mW	2N=14, R=10 GS/s	18 fj	2N=2000, R=10 GS/s	0.13 fj
DAC at 10 GHz for VCSELS	3.5 pJ/use (50, 51)	2N=14	0.25 pJ	2N=2000	1.7 fj
DAC at 10 GHz for LMNs	3.5 pJ/use (50, 51)	2M=14	0.25 pJ	2M=2000	1.7 fj
VCSEL AC driving	7 fj/use‡	2M=14	0.49 fj	2M=2000	3.5 aj
TFLN modulator AC driving	88 fj/use‡	2M=14	6.3 fj	2M=2000	40 aj
TIA+integrator	1 pJ/use(52)	2K=28x28x2	0.6 fj	2K=2000	0.5 fj
ADC at 10 MHz†	1 pJ/use(53)	2K=28x28x2	0.6 fj	2K=2000	0.5 fj
Total			525 fj/OP		4.6 fj/OP

‡TFLN modulator energy is calculated from the peak-to-peak driving voltage of 0.6 V with the 50 Ω load (Methods).
†The factor of 2 in parallelism accounts for the multiplication and accumulation operations.
†The system only readout once after integrating over 1000 time steps.

Table E2. Model size and accuracy of integrated optical systems

References	dataset	Input data size	Number of parameters in optics	Exp. accuracy
Shen 2017 (26)	Vowel	1x4	4x4 =16	76.7%
Feldmann 2021 (30)	MNIST	28x28 pixels	4x2x2 =16	95.3%
Ashtiani 2022 (32)	4-level EMNIST	3x4 pixels	3x4→3→2 =40	89.9%
Bandyopadhyay 2022 (27)	Vowel	1x6	6x6x3 =108	92.7%
Pai 2023 (25)	moons	64 pixels	4x4x3 =48	97%
Dong 2023 (31)	ECG dataset	1x35	3x1x3 =9	93.5%
This work	MNIST	28x28 pixels	28x28→10 =7,840	93.5%
	MNIST	28x28 pixels	28x28→100→10 =78,400	95.5%
	Fashion MNIST	28x28 pixels	28x28→100→10 =78,400	91.8%
	26-level EMNIST	28x28 pixels	28x28→500→26 =405,000	93.1%

Supplementary Information

HITOP multi-layer implementation

HITOP is an optoelectronic architecture. The input and weights are stored in nearby memories and transmitted to the optical system for matrix operations in the optical domain. The multiplied result is read out with charge accumulation and serialized with nonlinearity activation to the next layer. With a memory unit integrated together, our ONN could be used for multiple layer neural network inference with such working flow:

- Input vectors and weight vectors for the current layer are read out from the digital memory and programmed as time traces.
- Each input and weight time trace, respectively, is sent to the corresponding VCSEL or TFLN MZM (Fig. 1d).
- The output is acquired and accumulated by the photodetectors and time integrator arrays.
- Digital memory stores the spatially distributed signals from the photodetector and time integrator array.
- Reprogram the output by mapping the spatial distributed signal into corresponding time steps. The outputs of the same wavelength at different spatial channels are serialized as the input driving signal to a VCSEL transmitter in the next layer. Here the ReLU nonlinear operation function is encoded using the lasing threshold effect.

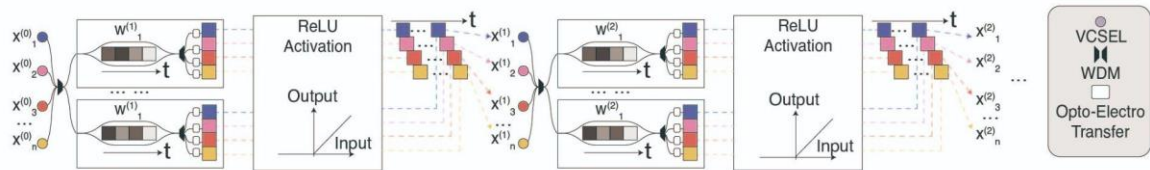


Fig. S1. HITOP forward propagating deep neural network architecture. The network consists of an arbitrary number of layers (2 layers are shown). Each layer computes a matrix-matrix multiplication in wavelength-time-space multiplexing using VCSELs and TFLN MZM (Fig. 1d).

TFLN Device characterization

Our MZMs are designed with slight imbalance path length between two arms, for the ease of calibration, which is not necessary in future full-system development. The free-spectral range is >150 nm, which is negligible in our demonstration with a total bandwidth of <5 nm.

The modulation function of lithium niobate is a sinusoidal function, which is quasi-linear when biasing at the quadrature point. The slight nonlinearity at close extinction point can be pre-calibrated with a linearity up to $>99.6\%$.

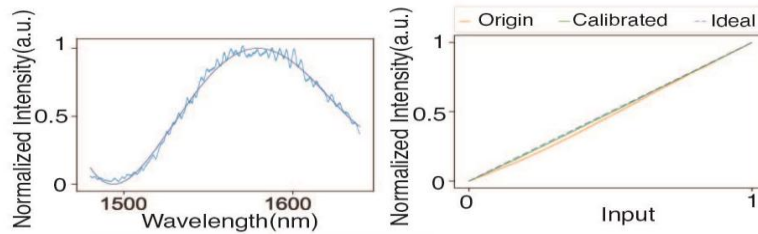


Fig. S2. TFLN MZM characteristics, left: the free spectrum range of a quasi-balance arm MZM, right: Linearity of the transfer function of the MZM, the standard deviation of the residue between calibrated transfer function and the ideal transfer function is less than 0.4%.

Data Encoding Accuracy

We investigate the encoding accuracy of our opto-electro transceiver, i.e. VCSEL and TFLN modulator, by applying random data distributed in the range of $[0,1]$. Due to the linearity of VCSEL response, when driving in the near-threshold region, we achieved 8-bit precision without extra calibration at low clock rates. With the linear calibration of MZM response, we also achieve 8-bit precision encoding accuracy with a single output TFLN MZM. Limited by our photodetectors and the measurement electronics, the encoding accuracy drops to 6 bits when the clock rate goes up to 10 GHz.

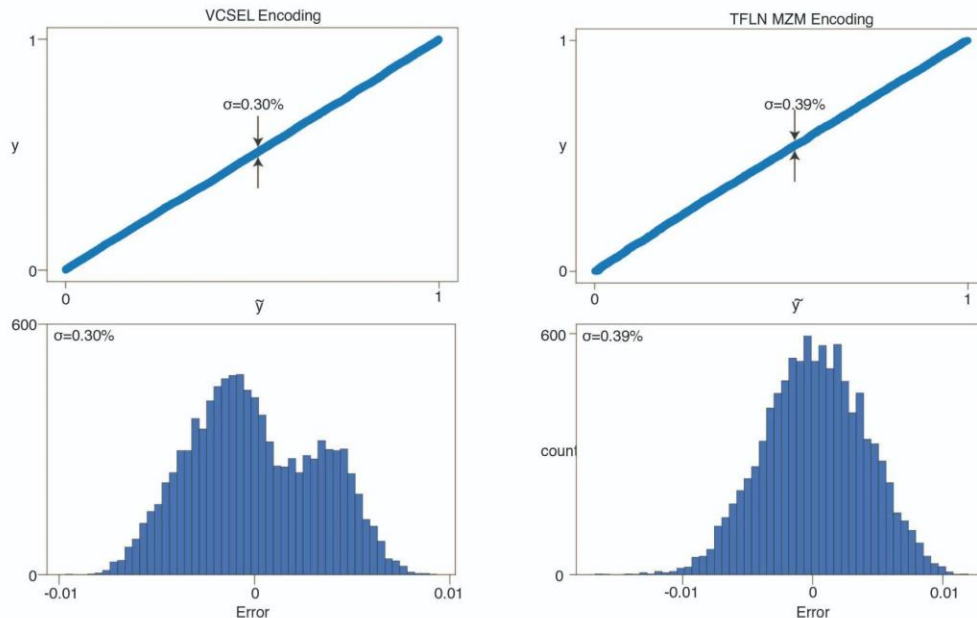
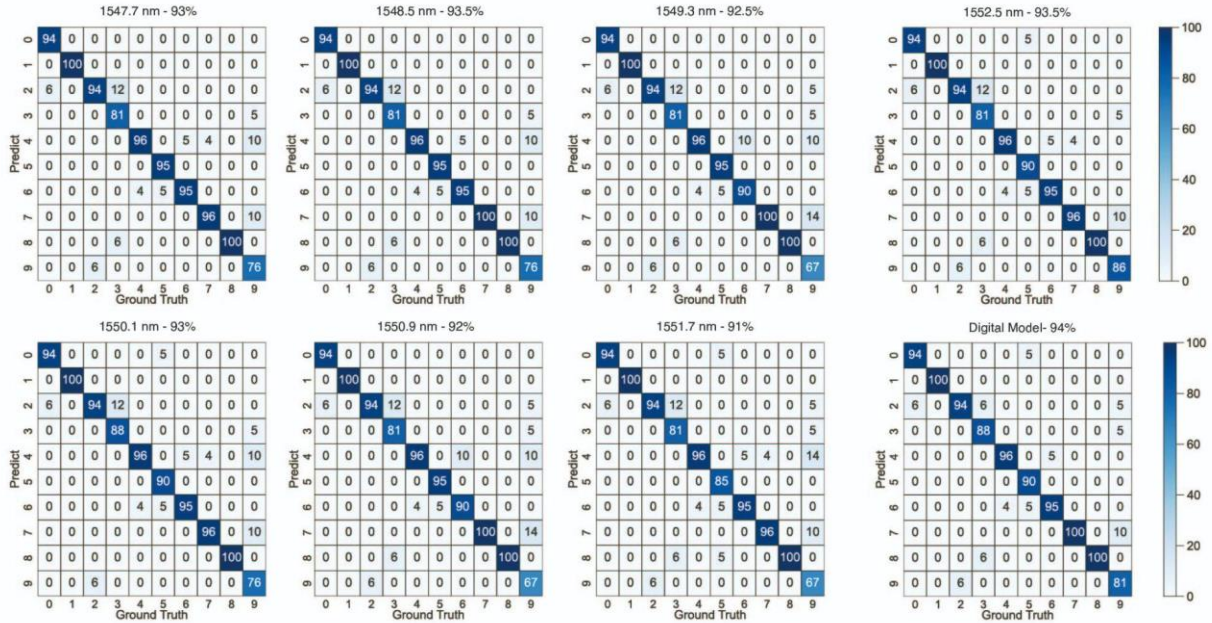


Fig. S3. Input-output voltage response accuracy of the VCSEL encoding and residuals (left) and TFLN MZM encoding (right) showing 8-bit precision.

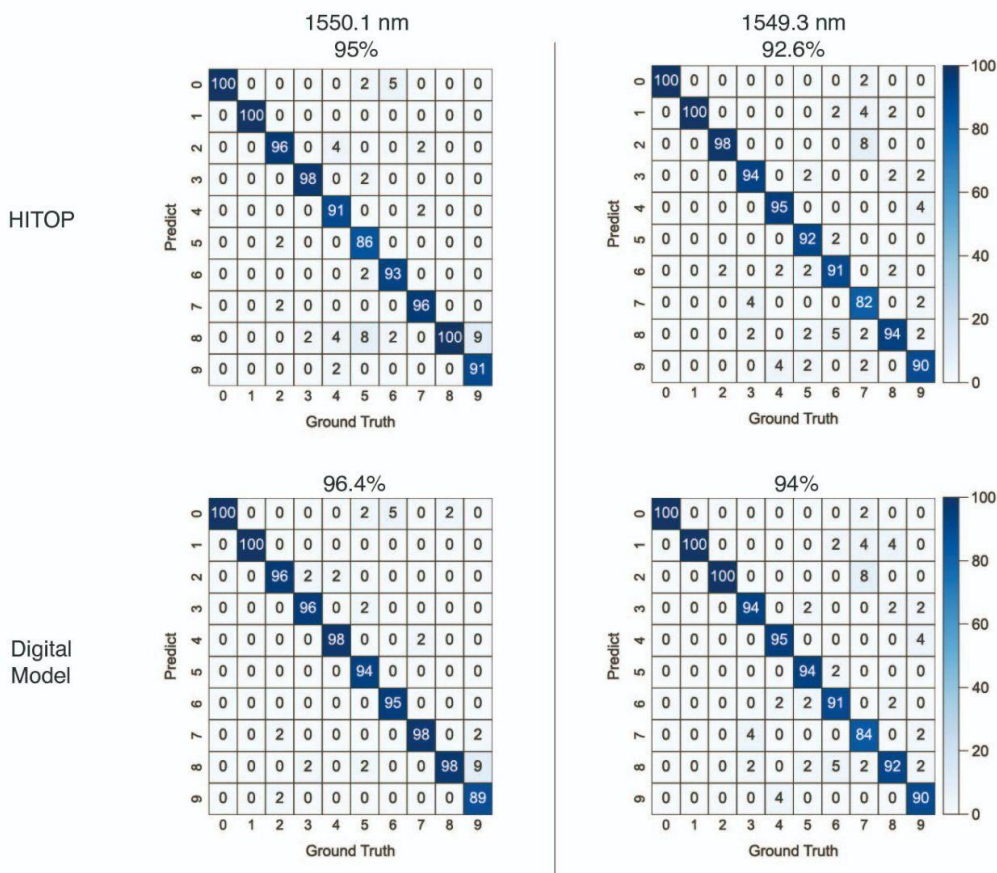
MNIST digit classification for multiple channels

To benchmark the optical bandwidth of HITOP. We randomly choose 200 MNIST images from the test set and perform inference on them using HITOP at 7 wavelengths with the 1-layer ANN. The wavelengths are selected to match the corresponding channels of our DWDM. The model has an inference accuracy of 94% while HITOP shows a similar performance at 7 wavelengths from 91% to 93.5%. Which is from 96.8% to 99.5% compared to the electronic inference.



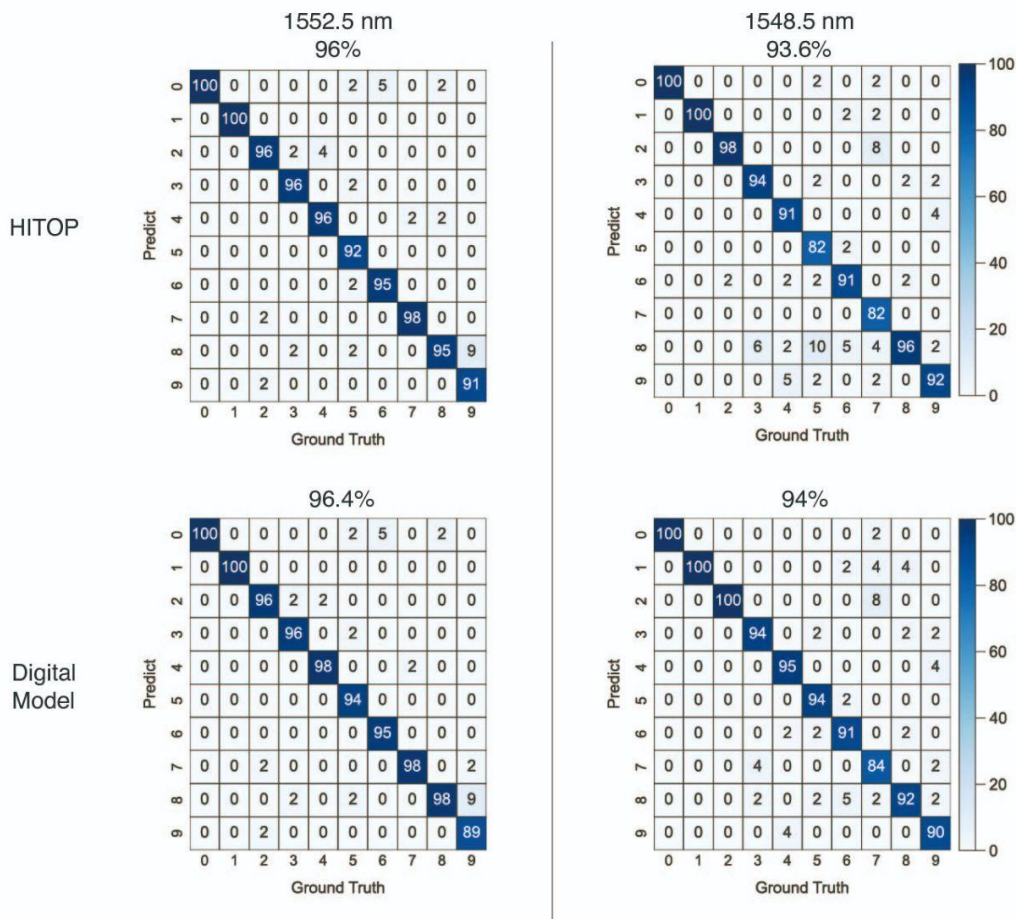
Figs. S5-1 HITOP confusion matrices with 200 MNIST test images at 7 wavelengths.

To verify the parallel computing accuracy of HITOP, we run the MNIST digit inferences with HITOP using 2 wavelength channels simultaneously. 2 sets of 500 MNIST images are randomly picked from the MNIST test dataset. Using the 2-layer DNN model, the electronic processor yields a 96.4% inference accuracy for the first set and 94% for the second set. Firstly, we sent to 2 VCSELs operating at 1549.3 nm and 1550.1 nm, which are the adjacent channels of the DWDM. HITOP shows 95% classification accuracy for the first set and 92.6% for the second set, which is 98.4% and 98.5% compared to the electronic inference.



Figs. S5-2 HITOP confusion matrices with 200 MNIST test images at 2 adjacent wavelengths.

We also perform the same inference using 2 further channels in our system at 1548.5 nm and 1552.5 nm. HITOP shows similar performance with 96% inference accuracy for the first set and 93.6% for the second set, which is 99.6% and 99.6% compared to the electronic inference.



Figs. S5-3 HITOP confusion matrices with 200 MNIST test images at 2 further wavelengths. All these benchmark tests verify that HITOP has the parallel computing ability and could have a large data throughput when operating at more wavelengths without a large deviation of the computing accuracy.

References

1. Y. LeCun, Y. Bengio, G. Hinton, Deep learning. *Nature*. **521**, 436–444 (2015).
2. OpenAI, GPT-4 Technical Report (2023), <http://arxiv.org/abs/2303.08774>.
3. A. Krizhevsky, I. Sutskever, G. E. Hinton, Imagenet classification with deep convolutional neural networks. *Adv. Neural Inf. Process. Syst.* **25** (2012).
4. Deep learning models for traffic flow prediction in autonomous vehicles: A review, solutions, and challenges. *Vehicular Communications*. **20**, 100184 (2019).
5. LimLek-Heng, Most Tensor Problems Are NP-Hard. *J. ACM* (2013).
6. Y. Saad, H. A. van der Vorst, Iterative solution of linear systems in the 20th century. *J. Comput. Appl. Math.* **123**, 1–33 (2000).
7. H.-C. Lin, Z. Wang, C. W. Hsu, Fast multi-source nanophotonic simulations using augmented partial factorization. *Nature Computational Science*. **2**, 815–822 (2022).
8. N. S. Bitcoin, Bitcoin: A peer-to-peer electronic cash system (2008).
9. A. Radford, K. Narasimhan, T. Salimans, I. Sutskever, Improving language understanding by generative pre-training, (available at Improving language understanding by generative pre-training).
10. P. P. Ray, ChatGPT: A comprehensive review on background, applications, key challenges, bias, ethics, limitations and future scope. *Internet of Things and Cyber-Physical Systems*. **3**, 121–154 (2023).
11. GPT-4. *Wikipedia*, <https://en.wikipedia.org/wiki/GPT-4> (2024).
12. V. Sze, Y.-H. Chen, T.-J. Yang, J. S. Emer, Efficient Processing of Deep Neural Networks: A Tutorial and Survey. *Proc. IEEE*. **105**, 2295–2329 (2017).
13. S. Markidis, S. W. D. Chien, E. Laure, I. B. Peng, J. S. Vetter, "NVIDIA Tensor Core Programmability, Performance & Precision" in *2018 IEEE International Parallel and Distributed Processing Symposium Workshops (IPDPSW)* (IEEE, 2018), pp. 522–531.
14. N. P. Jouppi, G. Kurian, S. Li, P. Ma, R. Nagarajan, L. Nai, N. Patil, S. Subramanian, A. Swing, B. Towles, C. Young, X. Zhou, Z. Zhou, D. Patterson, TPU v4: An Optically Reconfigurable Supercomputer for Machine Learning with Hardware Support for Embeddings. *arXiv: 2304.01433* (2023).
15. T. Chen, Z. Du, N. Sun, J. Wang, C. Wu, Y. Chen, O. Temam, DianNao: a small-footprint high-throughput accelerator for ubiquitous machine-learning. *SIGARCH Comput. Archit. News*. **42**, 269–284 (2014).
16. V. Sze, Y.-H. Chen, J. Emer, A. Suleiman, Z. Zhang, "Hardware for machine learning:

Challenges and opportunities" in *2017 IEEE Custom Integrated Circuits Conference (CICC)* (IEEE, 2017), pp. 1–8.

17. R. P. Feynman, Simulating physics with computers. *Int. J. Theor. Phys.* **21**, 467–488 (1982).
18. X. Lin, Y. Rivenson, N. T. Yardimci, M. Veli, Y. Luo, M. Jarrahi, A. Ozcan, All-optical machine learning using diffractive deep neural networks. *Science*. **361**, 1004–1008 (2018).
19. Tiankuang Zhou, Xing Lin, Jiamin Wu, Yitong Chen, Hao Xie, Yipeng Li, Jingtao Fan, Huaqiang Wu, Lu Fang and Qionghai Dai, Large-scale neuromorphic optoelectronic computing with a reconfigurable diffractive processing unit. *Nature Photonics*. **15**, 367–373 (2021).
20. L. G. Wright, T. Onodera, M. M. Stein, T. Wang, D. T. Schachter, Z. Hu, P. L. McMahon, Deep physical neural networks trained with backpropagation. *Nature*. **601**, 549–555 (2022).
21. T. Wang, S.-Y. Ma, L. G. Wright, T. Onodera, B. C. Richard, P. L. McMahon, An optical neural network using less than 1 photon per multiplication. *Nat. Commun.* **13**, 123 (2022).
22. L. Bernstein, A. Sludds, C. Panuski, S. Trajtenberg-Mills, R. Hamerly, D. Englund, Single-shot optical neural network. *Sci Adv.* **9**, eadg7904 (2023).
23. Z. Chen, A. Sludds, R. Davis, I. Christen, L. Bernstein, L. Ateshian, T. Heuser, N. Heermeier, J. A. Lott, S. Reitzenstein, R. Hamerly, D. Englund, Deep learning with coherent VCSEL neural networks. *Nat. Photonics*. **17**, 723–730 (2023).
24. R. Hamerly, L. Bernstein, A. Sludds, M. Soljačić, D. Englund, Large-Scale Optical Neural Networks Based on Photoelectric Multiplication. *Phys. Rev. X*. **9**, 021032 (2019).
25. S. Pai, Z. Sun, T. W. Hughes, T. Park, B. Bartlett, I. A. D. Williamson, M. Minkov, M. Milanizadeh, N. Abebe, F. Morichetti, A. Melloni, S. Fan, O. Solgaard, D. A. B. Miller, Experimentally realized in situ backpropagation for deep learning in photonic neural networks. *Science*. **380**, 398–404 (2023).
26. Yichen Shen, Nicholas C. Harris, Scott Skirlo, Mihika Prabhu, Tom Baehr-Jones, Michael Hochberg, Xin Sun, Shijie Zhao, Hugo Larochelle, Dirk Englund, Marin Soljacic, Deep learning with coherent nanophotonic circuits. *Nature Photonics*. **11**, 441–446 (2017).
27. S. Bandyopadhyay, A. Sludds, S. Krastanov, R. Hamerly, N. Harris, D. Bunandar, M. Streshinsky, M. Hochberg, D. Englund, Single chip photonic deep neural network with accelerated training. *arXiv: 2208.01623* (2022).
28. A. N. Tait, T. F. de Lima, E. Zhou, A. X. Wu, M. A. Nahmias, B. J. Shastri, P. R. Prucnal, Neuromorphic photonic networks using silicon photonic weight banks. *Sci. Rep.* **7**,

7430 (2017).

29. X. Xu, M. Tan, B. Corcoran, J. Wu, A. Boes, T. G. Nguyen, S. T. Chu, B. E. Little, D. G. Hicks, R. Morandotti, A. Mitchell, D. J. Moss, 11 TOPS photonic convolutional accelerator for optical neural networks. *Nature*. **589**, 44–51 (2021).
30. J. Feldmann, N. Youngblood, M. Karpov, H. Gehring, X. Li, M. Stappers, M. Le Gallo, X. Fu, A. Lukashchuk, A. S. Raja, J. Liu, C. D. Wright, A. Sebastian, T. J. Kippenberg, W. H. P. Pernice, H. Bhaskaran, Parallel convolutional processing using an integrated photonic tensor core. *Nature*. **589**, 52–58 (2021).
31. B. Dong, S. Aggarwal, W. Zhou, U. E. Ali, N. Farmakidis, J. S. Lee, Y. He, X. Li, D.-L. Kwong, C. D. Wright, W. H. P. Pernice, H. Bhaskaran, Higher-dimensional processing using a photonic tensor core with continuous-time data. *Nat. Photonics*. **17**, 1080–1088 (2023).
32. F. Ashtiani, A. J. Geers, F. Aflatouni, An on-chip photonic deep neural network for image classification. *Nature*. **606**, 501–506 (2022).
33. Z. Chen, A. Sludds, R. Davis, I. Christen, L. Bernstein, T. Heuser, N. Heermeier, J. A. Lott, S. Reitzenstein, R. Hamerly, D. Englund, Deep Learning with Coherent VCSEL Neural Networks. *arXiv: 2207.05329* (2022).
34. A. Sludds, S. Bandyopadhyay, Z. Chen, Z. Zhong, J. Cochrane, L. Bernstein, D. Bunandar, P. B. Dixon, S. A. Hamilton, M. Streshinsky, A. Novack, T. Baehr-Jones, M. Hochberg, M. Ghobadi, R. Hamerly, D. Englund, Delocalized photonic deep learning on the internet's edge. *Science*. **378**, 270–276 (2022).
35. P. Kharel, C. Reimer, K. Luke, L. He, M. Zhang, Breaking voltage–bandwidth limits in integrated lithium niobate modulators using micro-structured electrodes. *Optica, OPTICA*. **8**, 357–363 (2021).
36. E. Heidari, H. Dalir, M. Ahmed, V. J. Sorger, R. T. Chen, Hexagonal transverse-coupled-cavity VCSEL redefining the high-speed lasers. *Nanophotonics*. **9**, 4743–4748 (2020).
37. R. Jäger, M. Grabherr, C. Jung, R. Michalzik, G. Reiner, B. Weigl, K. J. Ebeling, 57% wallplug efficiency oxide-confined 850 nm wavelength GaAs VCSELs. *Electron. Lett.* **33**, 330–331 (1997).
38. A. V. Babichev, L. Y. Karachinsky, I. I. Novikov, A. G. Gladyshev, S. A. Blokhin, S. Mikhailov, V. Iakovlev, A. Sirbu, G. Stepniak, L. Chorchos, J. P. Turkiewicz, K. O. Voropaev, A. S. Ionov, M. Agustin, N. N. Ledentsov, A. Y. Egorov, 6-mW Single-Mode High-Speed 1550-nm Wafer-Fused VCSELs for DWDM Application. *IEEE J. Quantum Electron.* **53**, 1–8 (2017).
39. A. V. Babichev, L. Ya. Karachinsky, I. I. Novikov, A. G. Gladyshev, S. Mikhailov, V. Iakovlev, A. Sirbu, G. Stepniak, L. Chorchos, J. P. Turkiewicz, M. Agustin, N. N. Ledentsov, K. O. Voropaev, A. S. Ionov, A. Yu. Egorov, "Continuous wave and

modulation performance of 1550nm band wafer-fused VCSELs with MBE-grown InP-based active region and GaAs-based DBRs" in *Vertical-Cavity Surface-Emitting Lasers XXI* (SPIE, 2017), vol. 10122, pp. 50–55.

40. M. Zhang, C. Wang, P. Kharel, D. Zhu, M. Lončar, Integrated lithium niobate electro-optic modulators: when performance meets scalability. *Optica, OPTICA*. **8**, 652–667 (2021).
41. C. Wang, M. Zhang, X. Chen, M. Bertrand, A. Shams-Ansari, S. Chandrasekhar, P. Winzer, M. Lončar, Integrated lithium niobate electro-optic modulators operating at CMOS-compatible voltages. *Nature*. **562**, 101–104 (2018).
42. T. B. Brown, B. Mann, N. Ryder, M. Subbiah, J. Kaplan, P. Dhariwal, A. Neelakantan, P. Shyam, G. Sastry, A. Askell, S. Agarwal, A. Herbert-Voss, G. Krueger, T. Henighan, R. Child, A. Ramesh, D. M. Ziegler, J. Wu, C. Winter, C. Hesse, M. Chen, E. Sigler, M. Litwin, S. Gray, B. Chess, J. Clark, C. Berner, S. McCandlish, A. Radford, I. Sutskever, D. Amodei, Language Models are Few-Shot Learners. *arXiv: 2005.14165* (2020).
43. Boehm, Gerhard, Markus Ortsiefer, Robert Shau, Juergen Rosskopf, Christian Lauer, Markus Maute, Fabian Köhler, Felix Mederer, Ralf Meyer, and Markus-Christian Amann, InP-based VCSEL technology covering the wavelength range from 1.3 to 2.0 μm . *J. Cryst. Growth*. **251**, 748–753 (2003).
44. S. Xu, Z. Ren, B. Dong, J. Zhou, W. Liu, C. Lee, Mid-Infrared Silicon-on-Lithium-Niobate Electro-Optic Modulators Toward Integrated Spectroscopic Sensing Systems. *Advanced Optical Materials*. **11**, 2202228 (2023).
45. D. Zhu, L. Shao, M. Yu, R. Cheng, B. Desiatov, C. J. Xin, Y. Hu, J. Holzgrafe, S. Ghosh, A. Shams-Ansari, E. Puma, N. Sinclair, C. Reimer, M. Zhang, M. Lončar, Integrated photonics on thin-film lithium niobate. *Adv. Opt. Photon., AOP*. **13**, 242–352 (2021).
46. B. Desiatov, A. Shams-Ansari, M. Zhang, C. Wang, M. Lončar, Ultra-low-loss integrated visible photonics using thin-film lithium niobate. *Optica, OPTICA*. **6**, 380–384 (2019).
47. L. Chang, Y. Li, N. Volet, L. Wang, J. Peters, J. E. Bowers, Thin film wavelength converters for photonic integrated circuits. *Optica, OPTICA*. **3**, 531–535 (2016).
48. K. Luke, P. Kharel, C. Reimer, L. He, M. Loncar, M. Zhang, Wafer-scale low-loss lithium niobate photonic integrated circuits. *Opt. Express*. **28**, 24452–24458 (2020).
49. S. Moazeni, S. Lin, M. Wade, L. Alloatti, R. J. Ram, M. Popović, V. Stojanović, A 40-Gb/s PAM-4 Transmitter Based on a Ring-Resonator Optical DAC in 45-nm SOI CMOS. *IEEE J. Solid-State Circuits*. **52**, 3503–3516 (2017).
50. P. Caragiulo, O. E. Mattia, A. Arbabian, B. Murmann, "A Compact 14 GS/s 8-Bit Switched-Capacitor DAC in 16 nm FinFET CMOS" in *2020 IEEE Symposium on VLSI Circuits* (IEEE, 2020), pp. 1–2.

51. P. C. D. Murmann, DAC Performance Survey 1996-2020. *DAC Performance Survey 1996-2020* (2020), <https://github.com/pietro-caragiulo/survey-DAC>.
52. E. Yang, T. Lehmann, High Gain Operational Amplifiers in 22 nm CMOS, 2019 IEEE International Symposium on Circuits and Systems (ISCAS) (IEEE, 2019), pp. 1-5.
53. B. Murmann, ADC Performance Survey 1997-2023.